applied sciences

MDPI

Article

Analysis of Nonlinear Vibration in Permanent Magnet Synchronous Motors under Unbalanced Magnetic Pull

Ao Zhang, Yan Bai, Bo Yang and He Li *

School of Mechanical Engineering & Automation, Northeastern University, Shenyang 110819, China; zhangao2902@163.com (A.Z.); dbdx_by@163.com (Y.B.); yangbo5326@gmail.com (B.Y.)

* Correspondence: hli@mail.neu.edu.cn; Tel.: +86-24-8637-4338

Received: 1 December 2017; Accepted: 9 January 2018; Published: 15 January 2018

Abstract: The vibration and noise of permanent magnet synchronous motors (PMSM) are mainly caused by unbalanced magnetic pull (UMP). This paper aims to investigate nonlinear vibration in PMSMs. Firstly, the analytical model of the air-gap magnetic field with an eccentric rotor in PMSM is studied, and the analytical model is verified by the finite element method. Then the dynamic model of an offset rotor-bearing system is established, and the gyroscopic effect, nonlinear bearing force and UMP are taken into consideration. Finally, the dynamic characteristics of different static displacement eccentricities, rotor offsets and radial clearances are investigated in both the time domain and the frequency domain. The results show that the amplitudes of dynamic responses increase with the static displacement eccentricity and rotor offset and high integer multiples of rotating frequency appear with the increase of displacement eccentricity. The coupling effects of bearing force, unbalanced mass force and UMP are observed in the frequency domain, and the frequency components in the dynamic responses indicate that the bearings have an effect on the system.

Keywords: PMSM; unbalanced magnetic pull; nonlinear vibration; offset rotor bearing system; gyroscopic effect; coupling effects

1. Introduction

Permanent magnet synchronous motors (PMSM) have been used in many fields due to their many advantages, such as their fast response, high efficiency, and so on [1]. With their widespread applications, the vibration and failure of motors has been an important issue, and the failures can be divided into mechanical failure and electrical failure [2,3]. In general terms, the electromagnetic forces on the rotor surface are balanced when the air-gap distribution between the rotor and the stator is uniform [4]. However, the rotor is often eccentric with respect to the stator due to manufacturing tolerances, bearing wear and incorrect assembly, which means that the air-gap distribution is not uniform and the electromagnetic forces are imbalanced. Consequently, a net radial force, named unbalanced magnetic pull (UMP), is generated, and the UMP pulls the rotor towards to the stator in the direction of the minimum air-gap. The motion of the rotor can cause some vibrations and stability problems for the motor [5,6], and even cause the motor to fail and affect the normal operation of the entire system.

Generally speaking, the eccentricity between the rotor and stator can be classified into static eccentricity, dynamic eccentricity and a combination of the two [7,8]. With static eccentricity, the axis of the rotor and the stator is misaligned and the rotor rotates about its axis. With dynamic eccentricity, the rotor does not rotate about its own axis. The position of the minimal air-gap is fixed with static eccentricity, while it rotates with the rotor with dynamic eccentricity. The eccentricity is the main cause of UMP, and many researchers have studied UMP for decades. The approaches can be classified

into the analytical method and the finite element method. Some researchers use the finite element method to analyze the UMP for its convenience and efficiency, but the analytical method can identify the key factors and reasons in the production of UMP. In the early twentieth century, Behrend [9] assumed that the magnetic flux density was in proportion to the air-gap length and obtained the linear expression of UMP. Then, Covo [10] presented a new improved equation of UMP by considering the effects of magnetic saturation. The linear equation of UMP was often used in engineering and it also solved some practical problems, but the accuracy was not reliable if the eccentricity was large. In the 1960s, Funke [11] put forward the idea that the relationship between the UMP and the eccentricity was nonlinear and studied the influence of UMP on a synchronous machine. Belmans [12] presented the nonlinear analytical expression of UMP by expanding the air-gap permeance as a Fourier series. In recent years, many researchers have adopted the nonlinear analytical method to study the UMP, and the air-gap permeance approach was a commonly used method for calculating the magnetic flux density to obtain UMP. Guo [13] presented an analytical expression of the UMP with any pole-pairs by expanding the air-gap permeance as a Fourier series and studied the effects of the UMP on the vibration of the rotor system. Pennacchi [14,15] described a model based on the actual position of the rotor inside the stator and the model was more general than other models. Im [16] analyzed the dynamic behavior of a brushless direct-current (BLDC) motor when the motor was undergoing a mechanical and electromagnetic interaction due to the air-gap variation between the stator and rotor. Wu [17] studied the circular whirling and stability of a synchronous generator under the UMP and mass eccentric force. Gustavsson [5] presented an analytical model to study the influence of nonlinear magnetic pull on rotor stability for a synchronous hydropower generator. Chen [18] studied the UMP resulting from a non-uniform magnetic field and analyzed the nonlinear phenomenon vibrations for PMSM used in hybrid electric vehicles (HEV). Lundström [19] adopted a balanced Jeffcott rotor model of a hydropower generator and studied the dynamic consequences of UMP due to shape deviations on the rotor and stator. Xiang [20] investigated the nonlinear dynamic behaviors influenced by UMP and analyzed the stiffness characteristics of the rotor system of the PMSM based on a Jeffcott rotor model. Zhang [21] analyzed the dynamic characteristics of a rotor-bearing system considering the rub-impact on the hydraulic generating set under the UMP, and the analysis focused on the effects of the excitation current, eccentricity, and stiffness of shaft.

Almost all the papers mentioned above used a symmetrical Jeffcott rotor as a simplified model to analyze the dynamic characteristics of a PMSM. In many practical applications, the rotor is not always in the middle of the shaft, which means that the gyroscopic effect needs to be taken into consideration. Some researchers have studied the influence of the gyroscopic effect on the rotor system, and the results have showed that the influence cannot be ignored [22,23]. The models adopted in their research were based on the assumption that the supports were rigid. In a PMSM, the supports of the shaft are always elastic due to the influence of the bearings, and it is necessary to take these elastic supports into consideration.

The purpose of this paper is to investigate the nonlinear dynamic characteristics of the rotor-bearing system in a PMSM. In this paper, we consider the influence of UMP and the gyroscopic effect. In Section 2, the radial air-gap flux density of an eccentric rotor is analyzed based on the early research [24–27]. In Section 3, the dynamic model of the rotor bearing system is presented under the influence of UMP and bearing forces. In Section 4, the nonlinear dynamic characteristics of the system are investigated and the fourth-order Runge–Kutta method is employed to calculate the nonlinear responses. In addition, the effects of the static eccentricity, rotor offset and radial clearance are analyzed in detail. Finally, the conclusions of this study are presented in Section 5.

2. Analysis of the Radial Air-Gap Flux Density in a Permanent Magnet Synchronous Motor (PMSM)

2.1. Radial Air-Gap Flux Density without Eccentricity

In general terms, the air-gap flux density can be obtained by the superposition of a permanent magnet field and an armature interaction field [28]:

$$B_0(\alpha, t) = B_{\mathrm{PM}}(\alpha, t) + B_{\mathrm{arm}}(\alpha, t) \tag{1}$$

where α is the space angle of the rotor, $B_{\mathrm{PM}}(\alpha, t)$ is the permanent magnet field, and $B_{\mathrm{arm}}(\alpha, t)$ is the armature interaction field. It is commonly accepted that the radial component of the flux density is the main cause of UMP and the tangential component is negligible [13,14]. Therefore, only the radial component of the air-gap flux density in this study is considered. By considering the effect of stator slotting, the permanent magnet field and the armature interaction field can be expressed as follows [24]:

$$B_{\mathrm{PM}}(\alpha, t) = \lambda(\alpha) \sum_{n=1,3,5\ldots}^{\infty} B_{\mathrm{mr}} \cos(np\alpha - n\omega_e t) \tag{2}$$

$$B_{\mathrm{arm}}(\alpha, t) = \lambda(\alpha) \sum_{v=1,2,3\ldots}^{\infty} B_{\mathrm{ar}} \cos(pv\alpha \mp \omega_e t) \tag{3}$$

where $\lambda(\alpha)$ is the relative permeance, B_{mr} is the amplitude of the nth permanent magnet field, B_{ar} is the amplitude of the vth armature interaction field, ω_e is the electric angular frequency, and p is the number of pole-pairs. For the motors with an integral slot, $v = 6k \pm 1$, and the sign before ω_e is a minus when it takes a plus. The relative permeance can be written as [26]:

$$\lambda(\alpha) = \Lambda_0 + \sum_{\mu=1}^{\infty} \Lambda_\mu \cos \mu Z(\alpha + \pi/Z) \tag{4}$$

where Z is the slot number, Λ_0 is the fundamental amplitude of relative permeance, and Λ_μ is the harmonic amplitude of relative permeance.

Since the harmonic amplitude of relative permeance is very small and the effect on the rotor surface is negligible [26], the harmonic components can be neglected for the convenience of the latter calculation. Therefore, the radial air-gap flux density of a PMSM without eccentricity can be written as:

$$B_{r0}(\alpha, t) = \Lambda_0 \sum_{n=1,3,5\ldots}^{\infty} B_{\mathrm{mr}} \cos(np\alpha - n\omega_e t) + \Lambda_0 \sum_{v=1,2,3\ldots}^{\infty} B_{\mathrm{ar}} \cos(pv\alpha \mp \omega_e t) \tag{5}$$

2.2. Correction Factor of Relative Permeance

The air-gap distribution is not uniform when the rotor is eccentric with respect to the stator, and the radial air-gap flux density along the rotor surface is also not uniform. Since the relative permeance is inversely proportional to the air-gap length and the eccentricity can only affect the relative permeance [29], the radial air-gap flux density of a PMSM with eccentricity can be obtained by introducing the correction factor based on the air-gap flux density of a PMSM without eccentricity.

The position of the stator and the rotor for a cross section in PMSM can be shown as in Figure 1, and the air-gap length can be obtained by calculation. C_0 is the geometrical center of the stator, C is the geometrical center of the rotor under static eccentricity, and C_r is the geometrical center of the rotor during the rotation. The distance between C_0 and C is r_0, which is the static eccentricity and $r_0 = \sqrt{x_0^2 + y_0^2}$. The distance between C_r and C is r, which represents the dynamic eccentricity and $r = \sqrt{x^2 + y^2}$. θ is the position angle of the dynamic eccentricity and $\cos\theta = x/r$, $\sin\theta = y/r$.

The distance between C_r and C_0 is e, which represents the composite eccentricity, and β is the position angle at the instant time. R_r is the radius of the rotor and R_s is the radius of the stator.

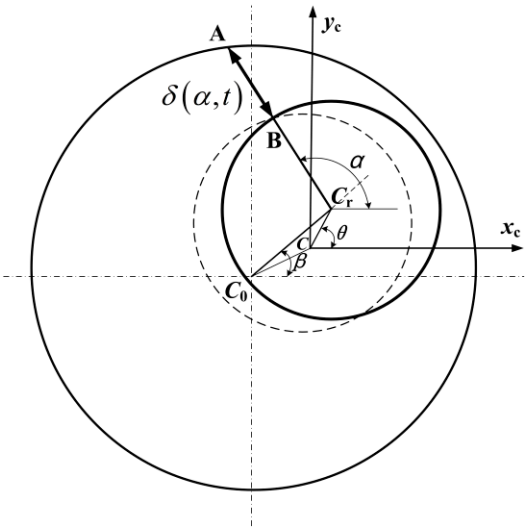


Figure 1. Air-gap for a cross section in a permanent magnet synchronous motor (PMSM).

In order to calculate the air-gap length, the geometrical relationship between the stator and the rotor needs to be investigated in detail. As Figure 1 shows, A is a point on the stator surface and B is a point on the rotor surface. The composite eccentricity can be written as follows:

$$e = |\mathbf{C_0C_r}| = \sqrt{(x + x_0)^2 + (y + y_0)^2} \tag{6}$$

The air-gap length can be calculated as:

$$\delta(\alpha, t) = l_{\mathrm{AB}} = l_{\mathrm{AC}_r} - R_r \tag{7}$$

Based on the cosine theorem, the length of AC_r can be written as:

$$l_{\mathrm{AC}_r} = \sqrt{{R_s}^2 - e^2 \sin^2(\alpha - \beta)} - e\cos(\alpha - \beta) \tag{8}$$

Considering $e^2 \ll R_s^2$, the length of AC_r can be approximately expressed as:

$$l_{\mathrm{AC}_r} \approx R_s - e\cos(\alpha - \beta) \tag{9}$$

Then the air-gap length can be obtained as follows:

$$\delta(\alpha, t) = R_s - R_r - e\cos(\alpha - \beta) = \delta_0 - e\cos(\alpha - \beta) \tag{10}$$

where δ_0 is the average air-gap length when the rotor is not eccentric with respect to the stator.

Considering the effect of the thickness of the magnet, the effective air-gap length can be expressed as [26]:

$$\delta' = \delta_0 + h_m/\mu_r \tag{11}$$

where h_m is the thickness of the magnet, and μ_r is the relative recoil permeability of the magnet.

According to Equations (10) and (11), the air-gap length can be written as follows:

$$\delta(\alpha, t) = \delta' - e\cos(\alpha - \beta) \tag{12}$$

where the position angle β can be written as:

$$\beta = \begin{cases} \arccos(\frac{x+x_0}{e}) & (y+y_0 \geq 0) \\ 2\pi - \arccos(\frac{x+x_0}{e}) & (y+y_0 < 0) \end{cases} \tag{13}$$

Since the relative permeance is inversely proportional to the air-gap length, the correction factor of the relative permeance ε can be calculated as:

$$\varepsilon = \frac{\delta'}{\delta(\alpha,t)} = \frac{\delta'}{\delta' - e\cos(\alpha-\beta)} = \frac{1}{1-\varepsilon'\cos(\alpha-\beta)} \tag{14}$$

where ε' is the relative eccentricity, and $\varepsilon' = e/\delta'$.

2.3. Radial Air-Gap Flux Density with Eccentricity

By introducing the correction factor ε, the radial air-gap flux density of PMSM with eccentricity can be obtained according to Equations (5) and (14).

$$B_r(\alpha,t) = [\Lambda_0 \sum_{n=1,3,5\ldots}^{\infty} B_{\mathrm{mr}}\cos(np\alpha - n\omega_e t) + \Lambda_0 \sum_{v=1}^{\infty} B_{\mathrm{ar}}\cos(pv\alpha \mp \omega_e t)] \times \varepsilon \tag{15}$$

In order to verify the analytical model of the radial air-gap flux density, the results are compared with the finite element model. Ansoft Maxwell is the leading software for the simulation of electromagnetic fields and it is based on the method of finite elements. The RMxprt module in Ansoft Maxwell includes many kinds of motors and it is very convenient for the calculation of electromagnetic fields. The model of PMSM in this paper was established by the RMxprt module and the main parameters are as shown in Table 1. Figure 2 shows the models for different pole-pair numbers in the finite element method (FEM). Based on the assumption that the static eccentricity is 1 mm and the dynamic eccentricity is ignored, the radial air-gap flux density of PMSM with different pole-pair numbers is calculated by the analytical model and the finite element model, and the results are shown in Figure 3. Figure 3a shows the distribution of the radial air-gap flux density on the rotor surface at a given time, and it is nonuniform due to the eccentricity. It can be seen that the analytical results are basically consistent with the finite element results. There are also some slight differences between the FEM and analytical waveforms at some space positions and the reason for them is the effect of stator slotting in the calculation of FEM. The field distribution in the air-gap will be affected due to the stator slotting [26], however, these differences do not have a great impact on the dynamic model. For convenience of calculation, the effect of stator slotting is ignored in the analytical method. Figure 3b shows the distribution of the radial air-gap flux density at a given point on the rotor surface in the time history. In the time history, the distribution varies periodically with time and the time for the rotor rotates with one pole-pair as one period. Since the rotating frequency is 25 Hz, the period of the field distribution is 0.04 s (p = 1), 0.02 s (p = 2) and 0.01 s (p = 4), respectively. It can also be seen that the analytical results are basically consistent with the finite element results and there are also some slight differences between them due to the effects of stator slotting. Therefore, the analytical model of the radial air-gap flux density is verified and can be used in the following study.

Table 1. Main parameters of PMSM.

Parameter	Value
Outer radius of the rotor core (R_r)	80 mm
Inner radius of the stator core (R_s)	92.5 mm
Pole-arc/pole-pitch ratio (α_p)	0.85
Slot-opening (b_0)	4 mm
Vacuum permeability (μ_0)	$4\pi \times 10^{-7}$ H/m
Current amplitude (I)	10 A
Slot number (Z)	48

Table 1. *Cont.*

Parameter	Value
Magnet thickness (h_m)	10 mm
Magnet remanence (B_r)	1.25 T
Relative recoil permeability (μ_r)	1.05
Rotor rotational speed (n)	1500 r/min
Length of the stator core	165 mm
Outer radius of the stator core	135 mm
Steel type of the stator core	DW315_50
Slot type of the stator core	No. 2
Number of winding layers	1
Winding type	Whole-Coiled
Number of parallel branches of stator winding	1
Conductors per slot	50
Inner radius of the rotor core	35 mm
Steel type of the rotor core	DW315_50
Length of the rotor core	165 mm
Stacking factor of the rotor core	0.95

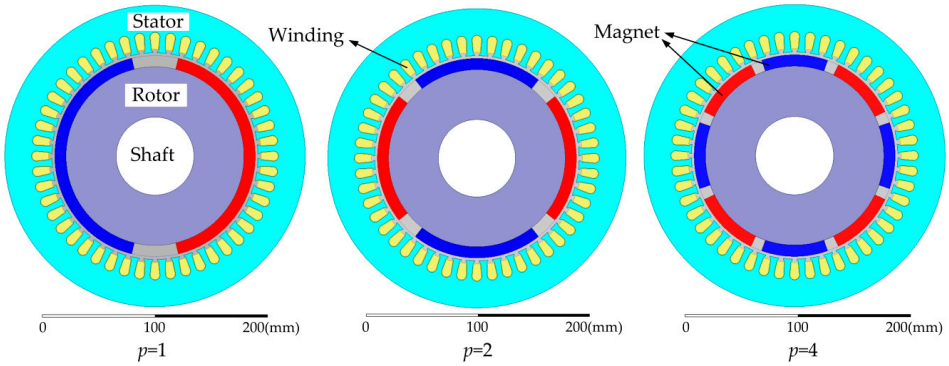


Figure 2. Models of PMSM for different pole-pair numbers.

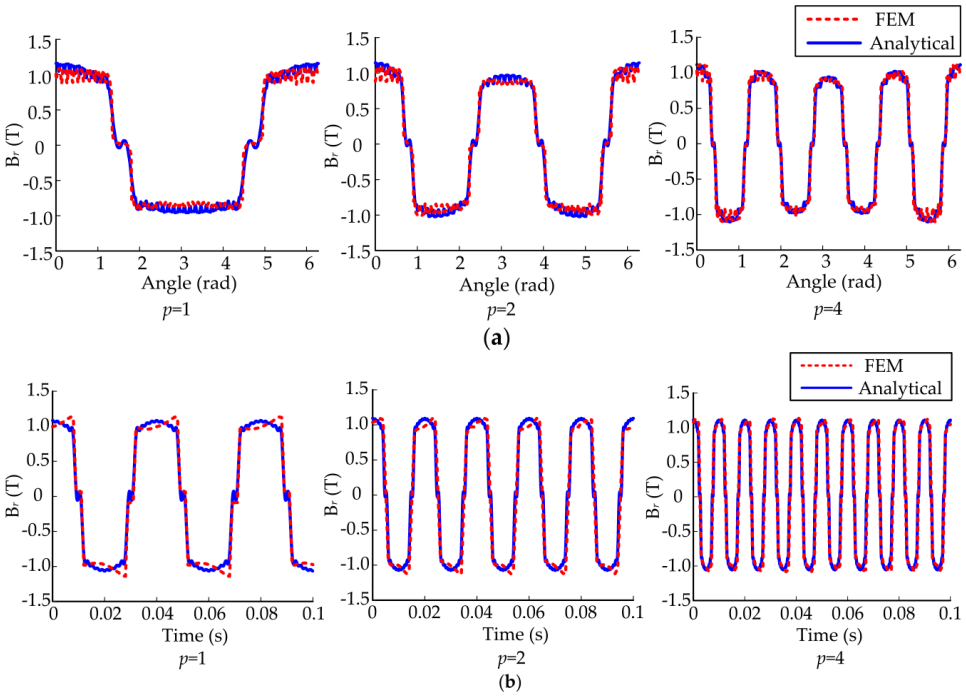


Figure 3. Comparison of field distribution on the rotor surface. (**a**) Field distribution at a given time; (**b**) Field distribution at a given point in time history. FEM: finite element method.

3. Dynamic Model of a Rotor Bearing System

3.1. Unbalanced Magnetic Pull (UMP) Model of Rotor

It is commonly accepted that the tangential component of flux density is negligible. Therefore, the radial Maxwell stress tensor can be expressed as [28]:

$$\sigma_r(\alpha, t) \approx \frac{B_r^2(\alpha, t)}{2\mu_0} = \frac{B_{r0}^2(\alpha, t)\varepsilon^2}{2\mu_0} \tag{16}$$

The radial Maxwell stress on the rotor surface can be obtained from Equation (16) and the pole-pair number here is one. Figure 4 shows the distribution and spectrum of the stress. It can be seen that the distribution is nonuniform when the eccentricity exists, and this leads to the appearance of UMP. The radial Maxwell stress is periodic in the time domain and the period is half of the radial air-gap flux density due to the square sign of Equation (16). Since the rotating frequency is 25 Hz and the pole-pair number is one, the period of the radial Maxwell stress is 0.02 s. The frequency components of the stress are integer multiples of 50 Hz. According to the working principle of PMSM, the rotating frequency multiplied by the pole-pair number is the power frequency. Thus, the power frequency here is 25 Hz and the frequency components of stress can be seen as the even multiples of power frequency. Actually, the analytic expression of Maxwell stress in the accepted literature [13] indicated that the frequency components of radial Maxwell stress were even multiples of power frequency. Therefore, the results in this study are in agreement with the reference.

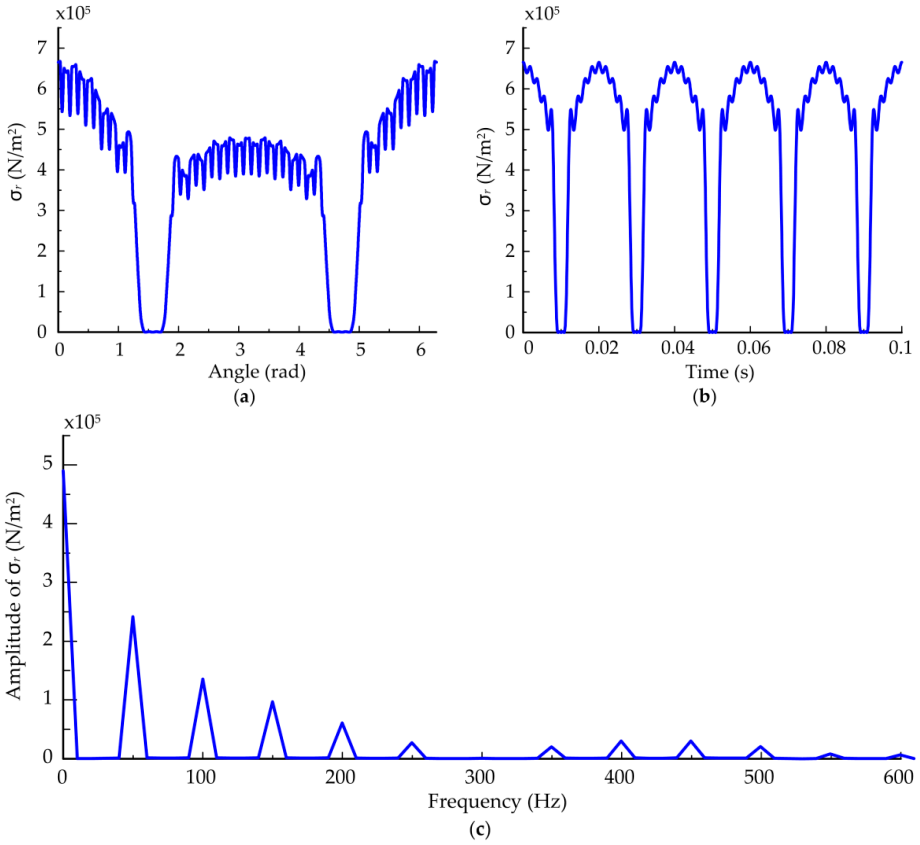


Figure 4. Distribution and spectrum of the radial Maxwell stress. (**a**) Stress distribution at a given time; (**b**) Stress distribution at a given point in time history; (**c**) Spectral characteristics of the stress.

Since the radial Maxwell stress is not uniform, the UMP is generated [30]. The UMP in the horizontal and vertical direction can be obtained by integrating the Maxwell stress along the spatial angle:

$$\begin{cases} F_{x\mathrm{UMP}} = R_r L \int_0^{2\pi} \sigma_r(\alpha, t) \cos\alpha \mathrm{d}\alpha \\ F_{y\mathrm{UMP}} = R_r L \int_0^{2\pi} \sigma_r(\alpha, t) \sin\alpha \mathrm{d}\alpha \end{cases} \tag{17}$$

where R_r is the radius of the rotor, and L is the length of the rotor.

3.2. Ball-Bearing Forces

Ball bearings are adopted in this study, and the ball-bearing forces can be obtained as follows [31]:

$$\begin{cases} F_x = -C_b \sum_{j=1}^{N_b} {\delta_j}^{3/2} H(\delta_j) \cos\theta_j \\ F_y = -C_b \sum_{j=1}^{N_b} {\delta_j}^{3/2} H(\delta_j) \sin\theta_j \end{cases} \tag{18}$$

where $\delta_j = x\cos\theta_j + y\sin\theta_j - \gamma$, $\theta_j = \frac{2\pi}{N_b}(j-1) + \omega_b t$, $j = 1, \ldots, N_b$, $H(\delta_j) = \begin{cases} 1, & \delta_j > 0 \\ 0, & \delta_j \le 0 \end{cases}$ is a heaviside function which shows the contact situation between the balls and outer ring of the bearing, and C_b is the Hertzian contact stiffness.

3.3. Equations of Motion

In this paper, the rotor bearing system is established in Figure 5, and the gyroscopic effect, nonlinear ball bearing forces and UMP are taken into consideration. The mass of the shaft is ignored and the parameters involved are expressed in Table 2. Based on Newton's second law, the equations of motion of the rotor bearing system can be deduced as:

$$\boldsymbol{M}\ddot{\boldsymbol{u}}^{\mathrm{T}} + (\Omega\boldsymbol{J} + \boldsymbol{C})\dot{\boldsymbol{u}}^{\mathrm{T}} + \boldsymbol{K}\boldsymbol{u}^{\mathrm{T}} = \boldsymbol{F} \tag{19}$$

where $\boldsymbol{u} = (x, \theta_y, x_A, x_B, y, \theta_x, y_A, y_B)$ is the generalized coordinate vector, $\boldsymbol{M} = \begin{pmatrix} \boldsymbol{M}_1 & \boldsymbol{0} \\ \boldsymbol{0} & \boldsymbol{M}_1 \end{pmatrix}$ is the mass matrix, $\boldsymbol{J} = \begin{pmatrix} \boldsymbol{0} & \boldsymbol{J}_1 \\ -\boldsymbol{J}_1 & \boldsymbol{0} \end{pmatrix}$ is the gyroscopic matrix, $\boldsymbol{K} = \begin{pmatrix} \boldsymbol{K}_1 + \boldsymbol{K}_b & \boldsymbol{0} \\ \boldsymbol{0} & \boldsymbol{K}_1 + \boldsymbol{K}_b \end{pmatrix}$ is the stiffness matrix and $\mathbf{C} = \begin{pmatrix} \boldsymbol{C}_1 & \boldsymbol{0} \\ \boldsymbol{0} & \mathbf{C}_1 \end{pmatrix}$ is the damping matrix. $\boldsymbol{M}_1, \boldsymbol{J}_1, \boldsymbol{K}_1, \boldsymbol{K}_b$ and $\boldsymbol{C}_1$ can be expressed as follows:

$$\begin{aligned} \boldsymbol{M}_1 &= \begin{pmatrix} m_d & & & \\ & J_d & & \\ & & m_A & \\ & & & m_B \end{pmatrix} \quad \boldsymbol{J}_1 = \begin{pmatrix} 0 & & & \\ & J_p & & \\ & & 0 & \\ & & & 0 \end{pmatrix} \\ \boldsymbol{K}_1 &= \begin{pmatrix} \boldsymbol{K}_c & -\boldsymbol{K}_c\boldsymbol{\Phi} \\ -\boldsymbol{\Phi}^{\mathrm{T}}\boldsymbol{K}_c & \boldsymbol{\Phi}^{\mathrm{T}}\boldsymbol{K}_c\boldsymbol{\Phi} \end{pmatrix} \quad \boldsymbol{K}_b = \begin{pmatrix} 0 & & & \\ & 0 & & \\ & & k_A & \\ & & & k_B \end{pmatrix} \\ \boldsymbol{C}_1 &= \begin{pmatrix} c & 0 & -\frac{c(-a+l)}{l} & -\frac{ac}{l} \\ 0 & c & \frac{c}{l} & -\frac{c}{l} \\ -\frac{c(-a+l)}{l} & \frac{c}{l} & \frac{c}{l^2} + \frac{c(-a+l)^2}{l^2} + c_b & -\frac{c}{l^2} + \frac{ac(-a+l)}{l^2} \\ -\frac{ac}{l} & -\frac{c}{l} & -\frac{c}{l^2} + \frac{ac(-a+l)}{l^2} & \frac{c}{l^2} + \frac{a^2c}{l^2} + c_b \end{pmatrix} \end{aligned} \tag{20}$$

where $J_p = J_d/2$ and $J_d = m_d R^2/2$. $\boldsymbol{\Phi}$ is the offset matrix which can be obtained by the geometrical relations of the rotor position:

$$\boldsymbol{\Phi} = \frac{1}{l}\begin{pmatrix} l-a & a \\ -1 & 1 \end{pmatrix} \tag{21}$$

$\boldsymbol{K}_c$ is the stiffness matrix when the supports are rigid, and can be obtained by the flexibility matrix method [32]:

$$\boldsymbol{K}_c = \left\{ \frac{1}{3EIl}\begin{pmatrix} a^2(l-a)^2 & a(l-a)(l-2a) \\ a(l-a)(l-2a) & l^2-3la+3a^2 \end{pmatrix} \right\}^{-1} \tag{22}$$

The external exciting force vector $\boldsymbol{F}$ of Equation (19) includes the unbalanced mass force, the ball-bearing force and the UMP. Therefore, the vector $\boldsymbol{F}$ can be written as

$$\begin{aligned} \boldsymbol{F} &= \boldsymbol{F}_1 + \boldsymbol{F}_2 + \boldsymbol{F}_3 \\ \boldsymbol{F}_1 &= \begin{pmatrix} m_d e_0 \Omega^2 \cos \Omega t & 0 & 0 & 0 & m_d e_0 \Omega^2 \sin \Omega t & 0 & 0 & 0 \end{pmatrix}^{\mathrm{T}} \\ \boldsymbol{F}_2 &= \begin{pmatrix} 0 & 0 & F_{Ax} & F_{Bx} & 0 & 0 & F_{Ay} & F_{By} \end{pmatrix}^{\mathrm{T}} \\ \boldsymbol{F}_3 &= \begin{pmatrix} F_{x\mathrm{UMP}} & 0 & 0 & 0 & F_{y\mathrm{UMP}} & 0 & 0 & 0 \end{pmatrix}^{\mathrm{T}} \end{aligned} \tag{23}$$

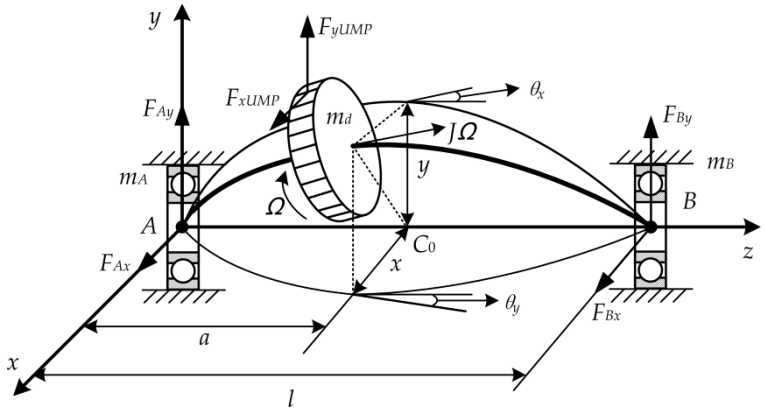


Figure 5. Dynamic model of the rotor bearing system.

Table 2. Parameters involved in the system.

m_A, m_B, mass of the bearings	m_d, mass of the rotor
a, distance between the rotor and the left bearing	l, length of the shaft
(x, y), position of rotor in coordinate system	(θ_x, θ_y), rotational angles of rotor
(x_A, y_A), position of left bearing in coordinate system	e_0, mass eccentricity of the rotor
(x_B, y_B), position of right bearing in coordinate system	Ω, rotating speed of the rotor
J_d, moment of inertia of rotor	J_p, polar moment of inertia of rotor
E, Young's modulus of the shaft	I, moment of inertia of shaft
c, damping of rotor	c_b, damping of bearings

4. Simulation Results and Analysis

Considering the strong nonlinear characteristics of the ball-bearing force and UMP, the numerical simulation is conducted by MATLAB, and the differential equations are solved by the fourth-order Runge–Kutta method. Furthermore, in order to eliminate the influence of the transient responses in the free vibration, the results of former periods are discarded and the last 400 periods are retained for analysis. The specific system parameters used are as follows: $m_d = 25$ kg, $m_A = m_B = 4$ kg, $c = 100$ N·s/m, $c_b = 200$ N·s/m, $EI = 0.819 \times 10^4$ N·m^2, $k_A = k_B = 2.5 \times 10^7$ N/m, $R_r = 0.08$ m, $L = 0.165$ m, $l = 0.75$ m, $e_0 = 10^{-4}$ m, $\Omega = 25$ Hz, $\delta' = 0.012$ m. The main parameters of the ball bearings are given in Table 3.

Table 3. Main parameters of the ball bearings.

Parameter	Value
Outer race radius (R_o)	63.9 mm
Inner race radius (R_i)	40.1 mm
Number of balls (N_b)	9
Radial clearance (γ)	10 μm
Hertzian contact stiffness (C_b)	1.334×10^{10} N/m$^{3/2}$

4.1. Effects of Static Displacement Eccentricity

Static displacement eccentricity always exists in rotating machinery due to many factors, such as the manufacturing tolerances and incorrect assembly. This kind of eccentricity can produce the UMP and vibrations. Therefore, it is necessary to study the effects of static displacement eccentricity on dynamic characteristics. The static displacement eccentricity in the x-direction is selected for analysis in this paper.

The rotor shaft orbits and bearing shaft orbits for different eccentricities are as shown in Figure 6. It is noted that the orbits of the rotor and bearings are similar and they are center circles when the static displacement eccentricity is zero. When the eccentricity exists, the orbits become irregular and larger. Since the static displacement eccentricity in the x-direction is selected in this study, the air-gap becomes short in the x-direction and the UMP pulls the rotor moving towards the stator in this direction. As a result, the orbits deviate from the origin with the increase in the eccentricity. From Figure 6b,c, we can see that the effects of the eccentricity on the left bearing are greater than the right due to the offset rotor, and this indicates that the bearing closer to the rotor can be affected more easily. It also can be seen that even a small eccentricity can cause a great variation for the orbits and this can cause vibration and motor noise, and a large eccentricity may produce a rub between the rotor and stator. Therefore, to avoid the appearance of rub, the static displacement eccentricity must to be monitored and controlled as much as possible.

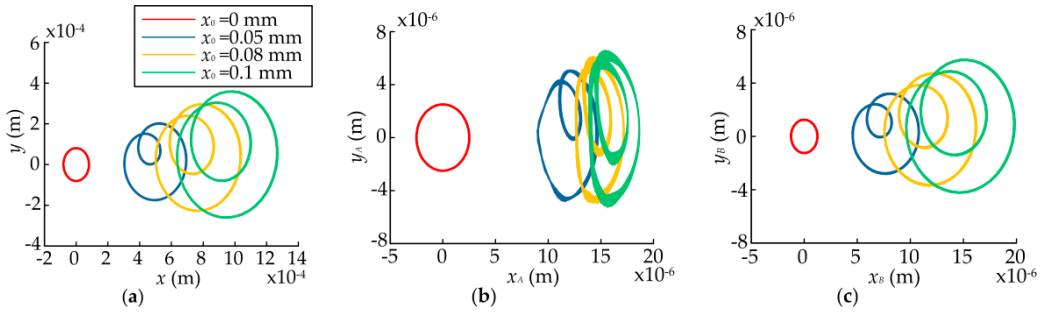


Figure 6. Rotor shaft orbits and bearing shaft orbits for different eccentricities. (**a**) Rotor shaft orbits; (**b**) Left-bearing shaft orbits; (**c**) Right-bearing shaft orbits.

The dynamic responses of the system for different eccentricities are displayed in Figure 7. With the increase of eccentricity, the dynamic responses increase nonlinearly due to the effects of UMP and bearing forces. In Figure 7a, the results show that both the displacement responses (x and y) and angle responses (θ_x and θ_y) increase when the eccentricity increases, and this phenomenon indicates that the displacement responses and angle responses are interactive. It can be seen clearly that the change regulations of x and θ_y are similar, and the change regulations of y and θ_x are also similar. The results are in agreement with the reference [23]. The reference also indicated that the averages of x and θ_y within one period deviated from zero and the averages of y and θ_x within one period remained zero when the eccentricity existed. However, in our investigation, the averages of both the dynamic displacement responses and angle responses within one period are not zero. This indicates

that the static displacement eccentricity in the x-direction can also affect the dynamic responses in the y-direction in our model. As Figure 7b shows, the dynamic responses of the bearings are similar in the same direction and the change regulations are similar with the displacement responses of the rotor. It is noted that the dynamic responses of the left bearing are clearly larger than the right when the eccentricity is small. If the eccentricity becomes a little larger, there will be little difference between the left and the right. The main cause of this phenomenon is the bearing forces. When the eccentricity is small, the dynamic responses and the radial deformations of the bearings are small. In this situation, the bearing forces will be very small and the dynamic responses of the bearings are mainly affected by the rotor. Thus, the bearing closer to the rotor will be affected more greatly and the dynamic responses will be larger. However, when the eccentricity becomes large, the bearing forces will be large with the increase of the radial deformation of the bearing. The effect of the bearing forces on the left bearing will gradually become larger and it will slow down the increase of dynamic responses. Through the above analysis, we can see the bearing forces can affect the dynamic responses of the system in some way.

The spectral characteristics of the dynamic responses are as shown in Figure 8. The results of the studied model in reference [13] indicated that the frequency components contained the rotating frequency, the double power frequency and the double power frequency minus the rotating frequency. It is noted that the main frequencies in Figure 8a,b are 0 Hz, 25 Hz and 50 Hz. Since the rotating frequency and power frequency are both 25 Hz in our research, the results can be seen as consistent with the results from reference [13]. The frequency components in Figure 8a also contain the integer multiples of rotating frequency when the eccentricity exists, which means that the eccentricity can produce large dynamic responses and excite high integer multiples of rotating frequency. It is commonly accepted that the varying compliance (VC) vibration from a ball bearing is an inevitable source of excitation to the rotor bearing system [33], and the VC frequency (f_{vc}) can be calculated by BN $\times$ Ω, where BN = $R_i \times N_b/(R_i + R_o)$ [34]. The value of BN depends on the dimensions of the bearing and is 3.47 in this study. It can be observed that the components of VC frequency minus integral multiples of rotating frequency exist in Figure 8a, which indicates that the bearing forces have an effect on the rotor system. Figure 8b displays the spectra of angle response in the x-direction and also contains the integral multiples of rotating frequency and the combined frequencies. It can be noticed that the frequency components of angle response are more complex than displacement response, which indicates that the eccentricity has a greater effect on the angle response. The combined frequencies $f_{\mathrm{vc}} - 3\Omega, f_{\mathrm{vc}} + 3\Omega, f_{\mathrm{vc}} + 5\Omega, f_{\mathrm{vc}} + 7\Omega$ and $f_{\mathrm{vc}} + 9\Omega$ are more obvious than other combined frequencies. From Section 3.1, we can see that the frequency components of radial Maxwell stress are the even multiples of power frequency. Thus, the combined frequencies $f_{\mathrm{vc}} - 3\Omega, f_{\mathrm{vc}} + 3\Omega, f_{\mathrm{vc}} + 5\Omega$, $f_{\mathrm{vc}} + 7\Omega$ and $f_{\mathrm{vc}} + 9\Omega$ can be seen as the combination of VC frequency, rotating frequency and even multiples of power frequency, from which it can be inferred that the coupling effects of bearing forces, unbalanced mass force and UMP obviously exist. Although the amplitudes of these combined frequencies are not large, the coupling interaction can also cause some unwanted vibrations and noises. The spectra of dynamic displacement and angle responses in the y-direction are similar to the spectra in the x-direction and the analysis will no longer be illustrated. The spectra of the dynamic displacement response of the left bearing (x_A) are displayed in Figure 8c. It can be noticed that the frequency components of the bearing are more complex when the static displacement eccentricity exists, while the frequency component is Ω when the static displacement eccentricity is zero. The bearing shaft orbit in Figure 6 indicates that the dynamic displacement responses of bearings are small when the eccentricity is zero and the bearing forces cannot be formed in this case. As the eccentricity increases, the dynamic displacement responses of bearings become large and the bearing forces are then formed. Thus, the frequency components become complex due to the effects of the bearing forces. It can be seen that the main frequencies are Ω and 2Ω, which means the vibration of a bearing is largely affected by the rotor. The other frequencies are the combination of VC frequency and rotating frequency due to the coupling effects. The spectra of the dynamic responses show that the coupling effects affect both the bearing and rotor.

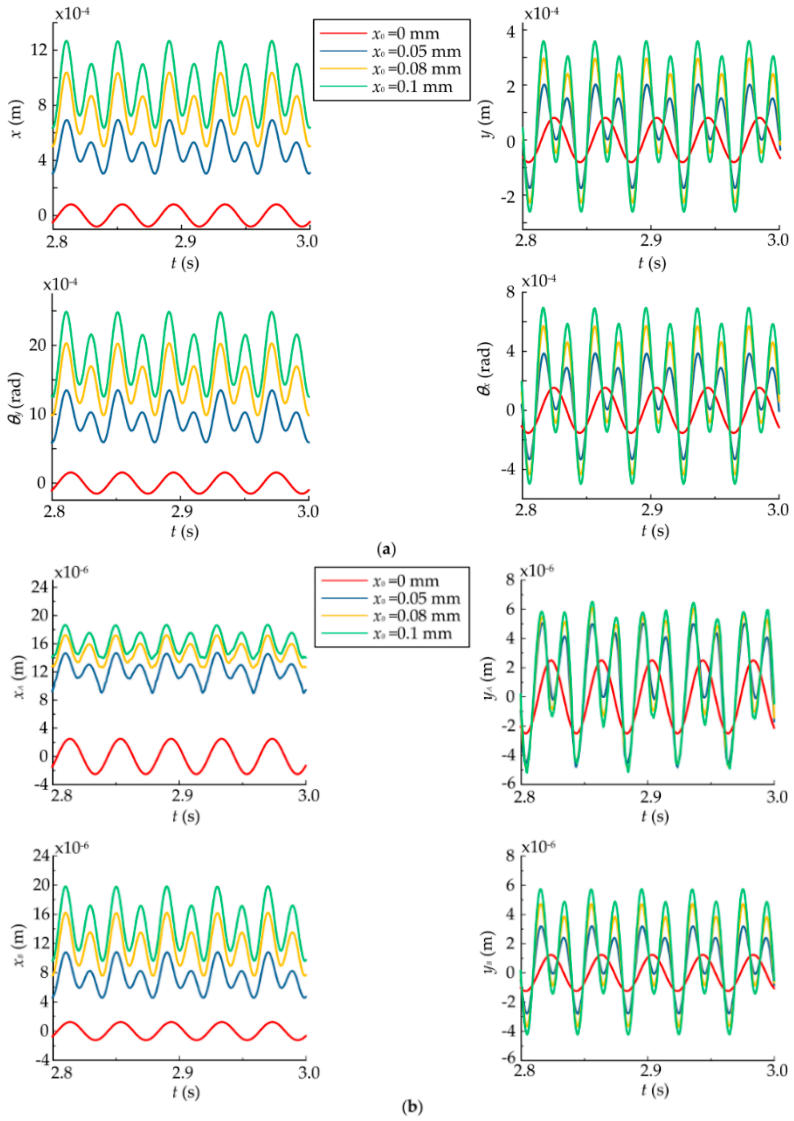


Figure 7. Time history of the dynamic responses for different eccentricities. (**a**) Time history of rotor dynamic responses; (**b**) Time history of bearing dynamic responses.

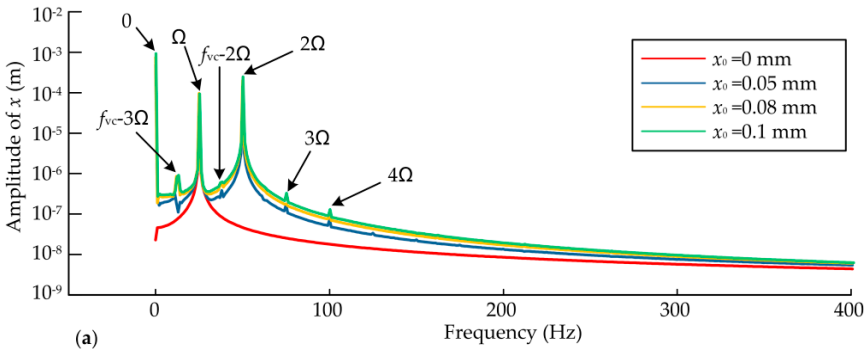


Figure 8. *Cont.*

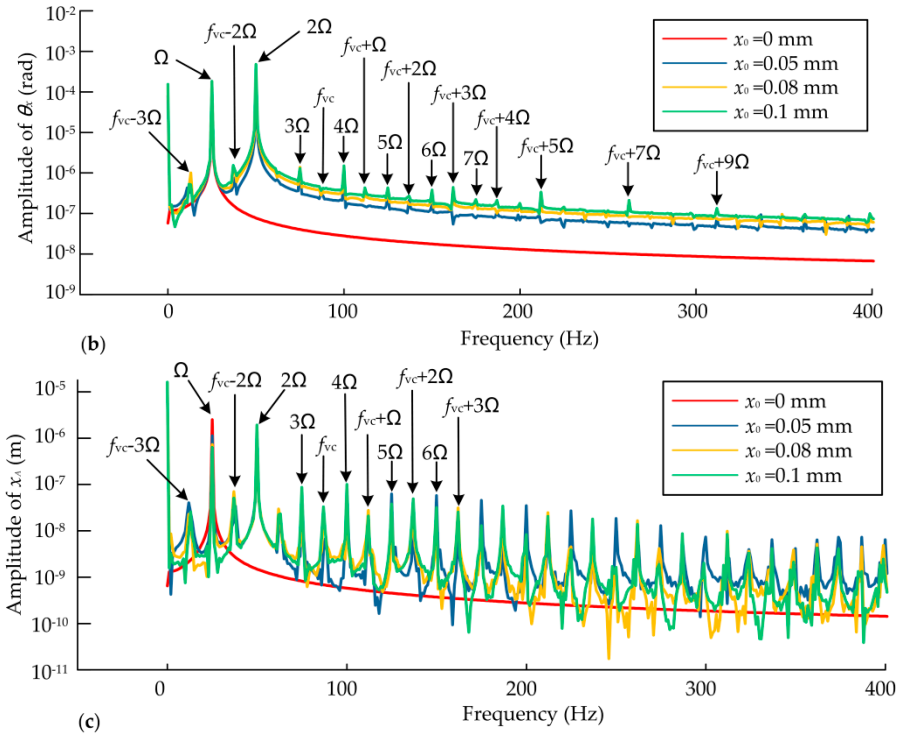


Figure 8. The spectra of dynamic responses for different static displacement eccentricities. (**a**) The spectra of x; (**b**) The spectra of θ_x; (**c**) The spectra of x_A.

4.2. Effects of Rotor Offset

In this section, the effects of different rotor offsets on the dynamic responses are studied. The static displacement eccentricity is ignored and the distance between the rotor and the left bearing A is set to be $a = 0.33l$, $a = 0.34l$, $a = 0.35l$ and $a = 0.36l$, respectively. The rotor shaft orbits and bearing shaft orbits for different rotor offsets are displayed in Figure 9. It can be seen that the orbits are center circles and they get smaller when the distance becomes large. Thus, in order to reduce the vibration, the rotor should be placed in the middle as much as possible. Figure 10 shows that the dynamic responses decrease with the distance and the change regulations in the x-direction and y-direction are similar. It can be inferred that the effects of rotor offset on the dynamic responses of the system are similar in the time domain. In Figure 11, the spectra of dynamic responses (x, θ_x and x_A) for different rotor offsets are displayed. It can be observed that the frequencies are simple when the static eccentricity is ignored. Figure 11a shows the spectra of x and the main frequency is Ω. The combination of VC frequency and rotating frequency can be observed when the rotor offset is $a = 0.33l$ and $a = 0.34l$, while the combined frequencies disappear when the rotor offset is $a = 0.35l$ and $a = 0.36l$. The spectra of θ_x in Figure 11b also show the same regulations and the combined frequencies are more obvious. The combined frequencies $f_{\mathrm{vc}} + 3\Omega$, $2f_{\mathrm{vc}} + 3\Omega$, $2f_{\mathrm{vc}} + 5\Omega$ and $3f_{\mathrm{vc}} + 5\Omega$ can also be seen as the combination of VC frequency, rotating frequency and even multiples of power frequency, which means the coupling effects of bearing forces, unbalanced mass force and UMP also exist when the rotor offset is $a = 0.33l$ and $a = 0.34l$. As Figure 9 shows, the dynamic responses of the bearings are larger when the rotor offset is $a = 0.33l$ and $a = 0.34l$, which means the radial deformations of the bearings are larger and the bearing forces will be formed. Thus, the coupling effects of bearing and rotor exist in these two cases, while the bearing forces cannot be formed and the coupling effects do not exist when $a = 0.35l$ and $a = 0.36l$. It also can be concluded that the coupling effects on the dynamic angle responses are greater than the displacement responses. In Figure 11c, the frequencies of x_A are similar to θ_x and they are more obvious when $a = 0.33l$ and $a = 0.34l$, which indicates that the coupling effects on the bearings are greater.

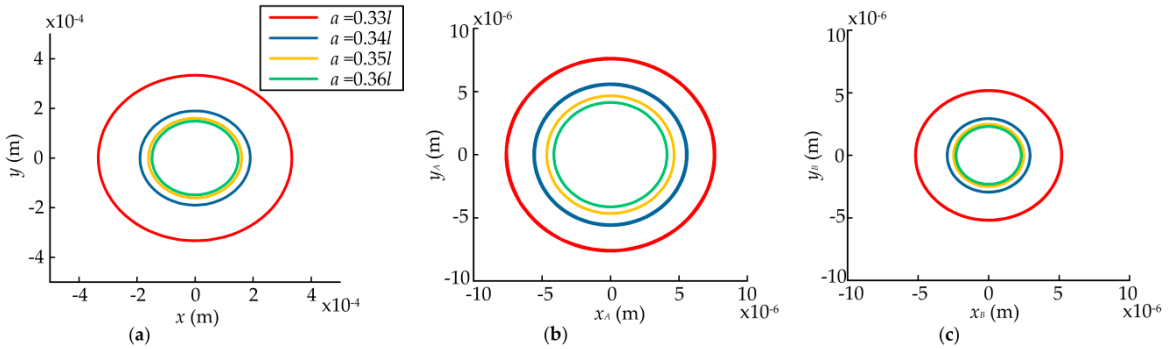


Figure 9. Rotor shaft orbits and bearing shaft orbits for different rotor offsets. (**a**) Rotor shaft orbits; (**b**) Left-bearing shaft orbits; (**c**) Right-bearing shaft orbits.

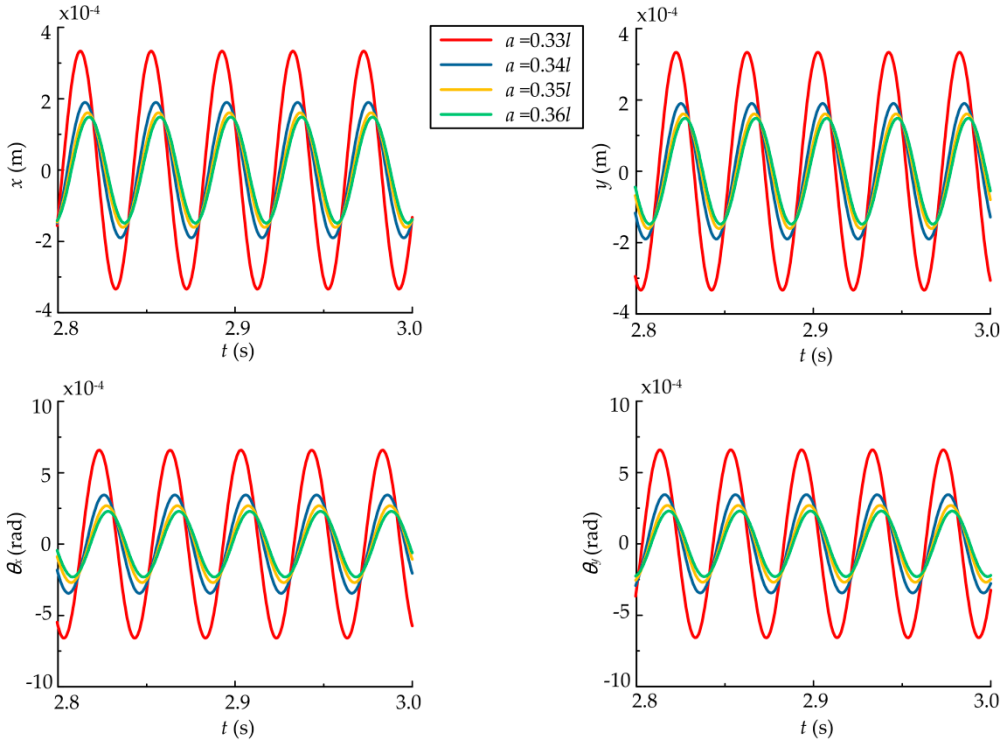


Figure 10. Time history of the dynamic responses for different rotor offsets.

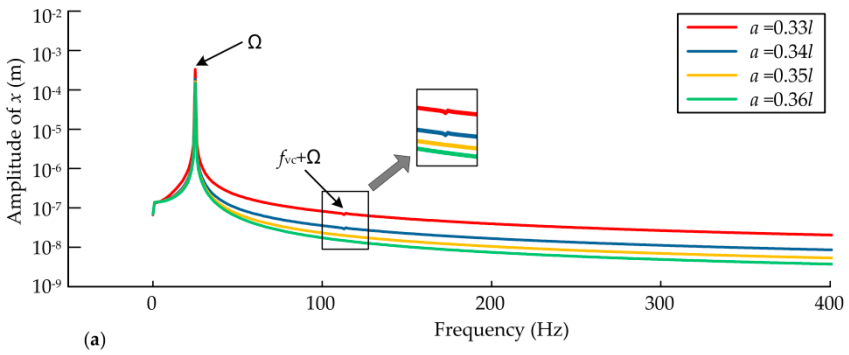


Figure 11. *Cont.*

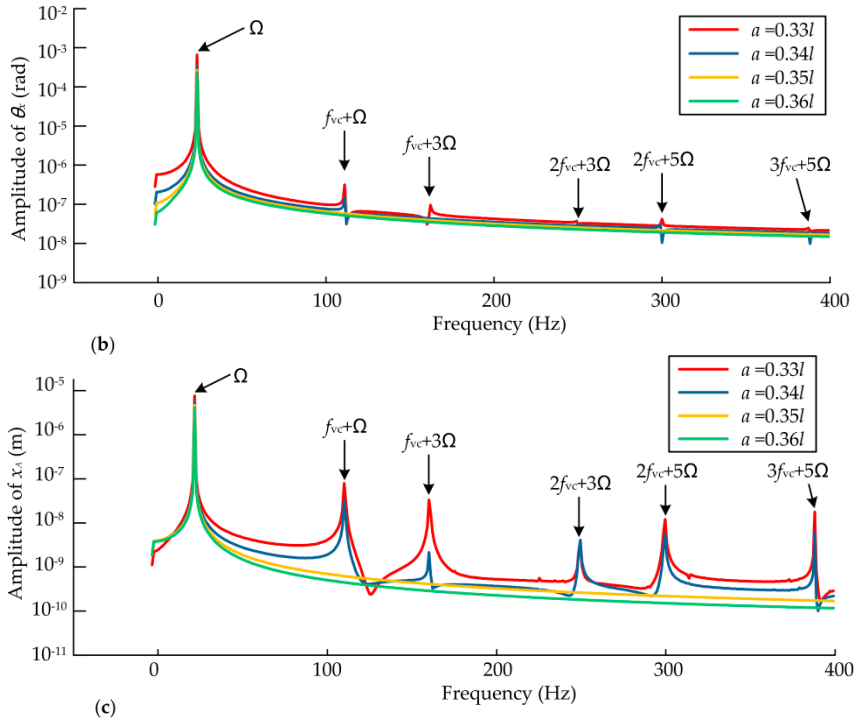


Figure 11. The spectra of dynamic responses for different rotor offsets. (**a**) The spectra of x; (**b**) The spectra of θ_x; (**c**) The spectra of x_A.

4.3. Effects of the Radial Clearance of Bearings

When the other conditions are the same, the shaft orbits for different radial clearances are displayed in Figure 12. It can be noticed that the orbits of the rotor and right bearing get smaller, while the orbits of the left bearing get bigger when the radial clearance is 1 μm, 3 μm, and 5 μm. When the radial clearance increases, the bearing forces become smaller and the bearing closer to the rotor is mainly affected by the rotor, while the bearing farther away from rotor is less affected by the rotor. As a consequence, the dynamic responses of the left bearing get larger due to the large dynamic responses of the rotor, while the dynamic responses of the right bearing get smaller. It can be inferred that the effects of radial clearance on the left and right bearing are different and the effects on the bearing closer to the rotor are greater than the other side. It also can be seen that the orbits are the same when the radial clearance is 5 μm and 10 μm. The reason for that is that the bearing forces cannot be formed when the radial clearance reaches a certain value and the effects of the bearing forces on the system do not exist under this situation.

From the time history of the rotor dynamic responses in Figure 13, we can know that the effects on the dynamic displacement responses and angle responses are similar. The spectra of dynamic responses for different radial clearances are displayed in Figure 14 and the combination of VC frequency and rotating frequency can be observed in Figure 14b,c. The combined frequencies $f_{vc} + 3\Omega$, $2f_{vc} + 3\Omega$, $2f_{vc} + 5\Omega$ and $3f_{vc} + 5\Omega$ indicate that the coupling effects of bearing forces, unbalanced mass force and UMP exist when the radial clearance is 1 μm and 3 μm, while the coupling effects disappear when the radial clearance is 5 μm and 10 μm. According to the above analysis, the bearing forces cannot be formed when the radial clearance reaches a certain value, and then the coupling effects disappear. It can also be inferred that the coupling effects on the angle responses are greater than the displacement responses and the coupling effects on the bearings are greater since the combined frequencies are more obvious. The combined frequencies are more obvious in the Figure 14c and this means that the coupling effects on the bearings are greater than the rotor.

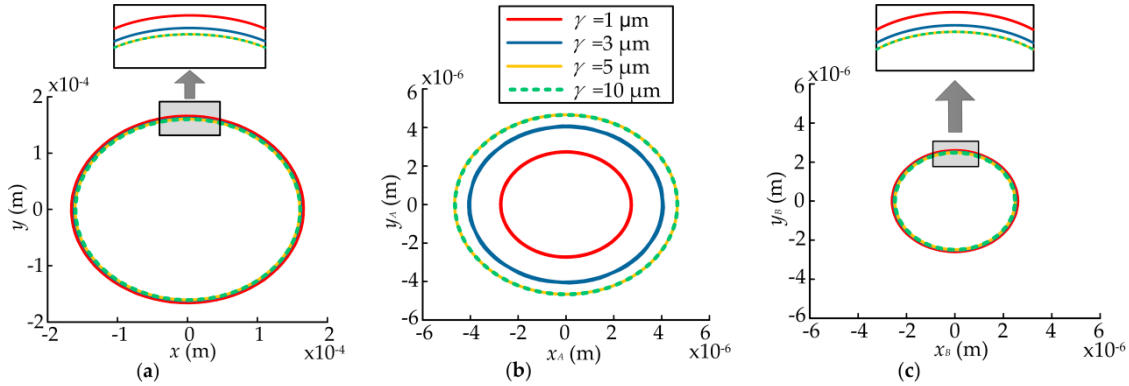


Figure 12. Rotor shaft orbits and bearing shaft orbits for different radial clearances. (**a**) Rotor shaft orbits; (**b**) Left-bearing shaft orbits; (**c**) Right-bearing shaft orbits.

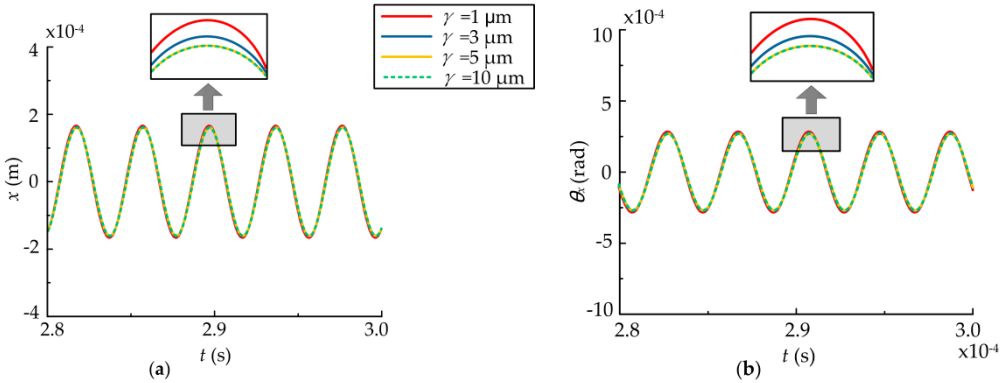


Figure 13. Time history of the dynamic responses for different radial clearances. (**a**) Time history of x; (**b**) Time history of θ_x.

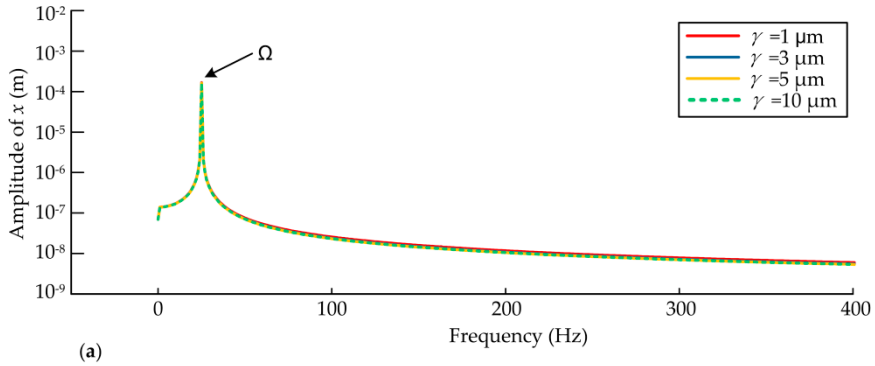


Figure 14. *Cont.*

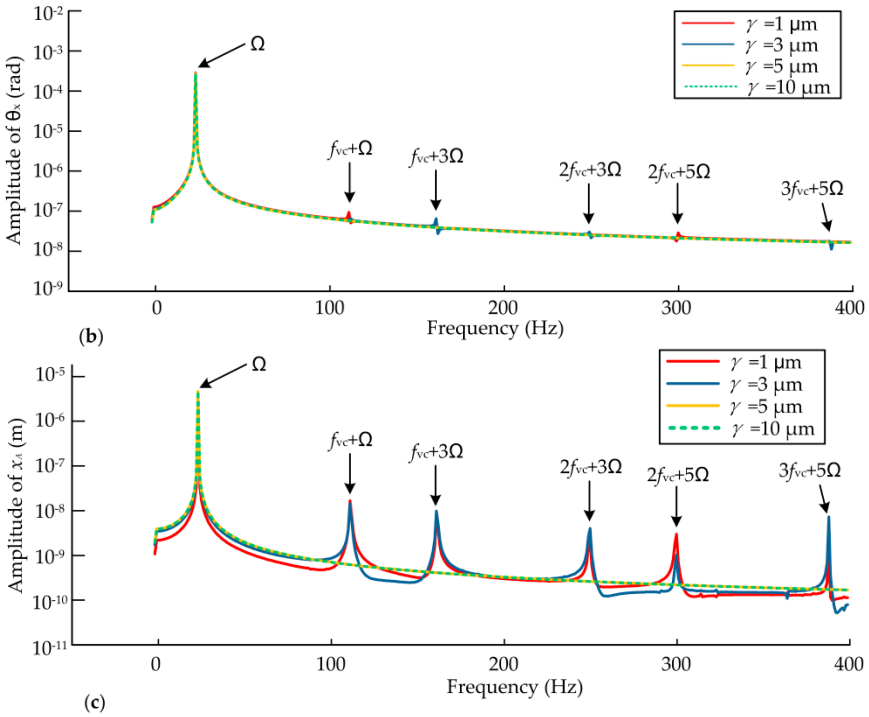


Figure 14. The spectra of dynamic responses for different rotor offsets. (**a**) The spectra of x; (**b**) The spectra of θ_x; (**c**) The spectra of x_A.*Cont*.

5. Conclusions

In this paper, the radial air-gap flux density of an eccentric rotor in a PMSM was analyzed and a dynamic model of a rotor bearing system was established when considering the gyroscopic effect, nonlinear bearing forces and UMP. The effects of static eccentricity, rotor offset and radial clearance on the system were analyzed in both the time domain and the frequency domain in detail. The main conclusions of this study can be summarized as follows:

1. The static displacement eccentricity has a great effect on the system and the orbits of the rotor and bearings are center circles when the static displacement eccentricity is zero, while they become irregular and lager when the eccentricity exists. The bearing closer to the rotor can be affected more easily when the rotor is not in the middle of the shaft. The dynamic responses increase nonlinearly with the eccentricity and rotor offset due to the effects of UMP and bearing forces. When the radial clearance increases within a certain range, the dynamic responses of the rotor and the bearing farther away from the rotor decrease, while the dynamic responses of the bearing closer to the rotor increase. When the radial clearance reaches a certain value, the dynamic responses of the system will no longer be changed since the effects of the bearings disappear.
2. The bearings have an effect on the system and the coupling effects of the bearing forces, unbalanced mass force and UMP are discovered in this study. The coupling effects exist when the bearing forces are formed, while the coupling effects disappear when the bearing forces are not formed. The dynamic angle responses are affected more obviously by the coupling effects than the displacement responses in the frequency domain.
3. The main frequencies of dynamic responses are the rotating frequency and the double rotating frequency when the static displacement eccentricity exists and the frequency components of the bearing are more complex, while the main frequency is the rotating frequency when the static eccentricity is zero. Moreover, high integer multiples of rotating frequency can be found with the increase of static displacement eccentricity. The combination of VC frequency and odd multiples

of rotating frequency can be observed more obviously than other combined frequencies due to the coupling effects, and the coupling effects on the bearings are greater.

Acknowledgments: This work was supported by the National Natural Science Foundation of China (Grant No. 51675091) and the Collaborative Innovation Center of Major Machine Manufacturing in Liaoning, the Major Scientific and Technological Innovation Project of Liaoning Province (Grant No. 201506003).

Author Contributions: Ao Zhang and Yan Bai conceived and designed the study; Ao Zhang and Bo Yang performed the simulation; Ao Zhang wrote the manuscript. He Li reviewed and edited the manuscript. All authors read and approved the manuscript.

Conflicts of Interest: The authors declare no conflict of interest.

References

1. Mehrjou, M.R.; Mariun, N.; Misron, N.; Radzi, M.A.M.; Musa, S. Broken Rotor Bar Detection in LS-PMSM Based on Startup Current Analysis Using Wavelet Entropy Features. *Appl. Sci.* **2017**, *7*, 845. [CrossRef]
2. Yang, H.; Chen, Y. Influence of Radial Force Harmonics with Low Mode Number on Electromagnetic Vibration of PMSM. *IEEE Trans. Energy Convers.* **2014**, *29*, 38–45. [CrossRef]
3. Kuo, C.; Liu, C.; Chang, H.; Lin, K. Implementation of a Motor Diagnosis System for Rotor Failure Using Genetic Algorithm and Fuzzy Classification. *Appl. Sci.* **2017**, *7*, 31. [CrossRef]
4. Pennacchi, P.; Frosini, L. Dynamical Behaviour of a Three-phase Generator due to Unbalanced Magnetic Pull. *IEE Proc. Electr. Power Appl.* **2005**, *152*, 1389–1400. [CrossRef]
5. Gustavsson, R.K.; Aidanpaa, J. The Influence of Nonlinear Magnetic Pull on Hydropower Generator Rotors. *J. Sound Vib.* **2006**, *297*, 551–562. [CrossRef]
6. Zhu, Z.Q.; Ishak, D.; Howe, D.; Chen, J. Unbalanced Magnetic Forces in Permanent-Magnet Brushless Machines with Diametrically Asymmetric Phase Windings. *IEEE Trans. Ind. Appl.* **2007**, *43*, 1544–1553. [CrossRef]
7. Calleecharan, Y.; Aidanpaa, J.O. Stability Analysis of an Hydropower Generator Subjected to Unbalanced Magnetic Pull. *IET Sci. Meas. Technol.* **2011**, *5*, 231–243. [CrossRef]
8. Ebrahimi, B.M.; Roshtkhari, M.J.; Faiz, J.; Khatami, S.V. Advanced Eccentricity Fault Recognition in Permanent Magnet Synchronous Motors Using Stator Current Signature Analysis. *IEEE Trans. Ind. Electron.* **2014**, *61*, 2041–2052. [CrossRef]
9. Behrend, A.B. On the Mechanical Forces in Dynamos Caused by Magnetic Attraction. *Trans. Am. Inst. Electr. Eng.* **1900**, *17*, 613–633. [CrossRef]
10. Covo, C. Unbalanced Magnetic Pull in Induction Motors with Eccentric Rotors. *Trans. Am. Inst. Electr. Eng.* **1954**, *73*, 1421–1425. [CrossRef]
11. Funke, H.; Maciosehek, G. Influence of Unbalanced Magnetic Pull on the Running of Synchronous Machine. *Electric* **1965**, *19*, 233–238.
12. Belmans, R.; Vandenput, A.; Geysen, W. Calculation of the Flux Density and the Unbalanced Pull in Two Pole Induction Machines. *Arch. Elektrotech.* **1987**, *70*, 151–161. [CrossRef]
13. Guo, D.; Chu, F.; Chen, D. The Unbalanced Magnetic Pull and its Effects on Vibration in a Three-Phase Generator with Eccentric Rotor. *J. Sound Vib.* **2002**, *254*, 297–312. [CrossRef]
14. Pennacchi, P. Computational Model for Calculating the Dynamical Behaviour of Generators Caused by Unbalanced Magnetic Pull and Experimental Validation. *J. Sound Vib.* **2008**, *312*, 332–353. [CrossRef]
15. Pennacchi, P. Nonlinear Effects Due to Electromechanical Interaction in Generators with Smooth Poles. *Nonlinear Dyn.* **2009**, *57*, 607–622. [CrossRef]
16. Im, H.; Hong, H.Y.; Chung, J. Dynamic Analysis of a BLDC Motor with Mechanical and Electromagnetic Interaction Due to Air Gap Variation. *J. Sound Vib.* **2011**, *330*, 1680–1691. [CrossRef]
17. Wu, B.; Sun, W.; Li, Z.; Li, Z. Circular Whirling and Stability Due to Unbalanced Magnetic Pull and Eccentric Force. *J. Sound Vib.* **2011**, *330*, 4949–4954. [CrossRef]
18. Chen, X.; Yuan, S.; Peng, Z. Nonlinear Vibration for PMSM Used in HEV Considering Mechanical and Magnetic Coupling Effects. *Nonlinear Dyn.* **2015**, *80*, 541–552. [CrossRef]
19. Lundström, N.L.P.; Aidanpaa, J. Dynamic Consequences of Electromagnetic Pull Due to Deviations in Generator Shape. *J. Sound Vib.* **2007**, *301*, 207–225. [CrossRef]

20. Xiang, C.; Liu, F.; Liu, H.; Han, L.; Zhang, X. Nonlinear Dynamic Behaviors of Permanent Magnet Synchronous Motors in Electric Vehicles Caused by Unbalanced Magnetic Pull. *J. Sound Vib.* **2016**, *371*, 277–294. [CrossRef]
21. Zhang, L.; Ma, Z.; Song, B. Dynamic Characteristics of a Rub-Impact Rotor-Bearing System for Hydraulic Generating Set Under Unbalanced Magnetic Pull. *Arch. Appl. Mech.* **2013**, *83*, 817–830. [CrossRef]
22. Gan, C.; Wang, Y.; Yang, S.; Cao, Y. Nonparametric Modeling and Vibration Analysis of Uncertain Jeffcott Rotor with Disc Offset. *Int. J. Mech. Sci.* **2014**, *78*, 126–134. [CrossRef]
23. Xu, X.; Han, Q.; Chu, F. A Four Degrees-Of-Freedom Model for a Misaligned Electrical Rotor. *J. Sound Vib.* **2015**, *358*, 356–374. [CrossRef]
24. Zhu, Z.Q.; Howe, D. Instantaneous Magnetic Field Distribution in Brushless Permanent Magnet DC Motors. I. Open-Circuit Field. *IEEE Trans. Magn.* **1993**, *29*, 124–135. [CrossRef]
25. Zhu, Z.Q.; Howe, D. Instantaneous Magnetic Field Distribution in Brushless Permanent Magnet DC Motors. II. Armature-Reaction Field. *IEEE Trans. Magn.* **1993**, *29*, 136–142. [CrossRef]
26. Zhu, Z.Q.; Howe, D. Instantaneous Magnetic Field Distribution in Brushless Permanent Magnet DC Motors. III. Effect of Stator Slotting. *IEEE Trans. Magn.* **1993**, *29*, 143–151. [CrossRef]
27. Zhu, Z.Q.; Howe, D. Instantaneous Magnetic Field Distribution in Permanent Magnet Brushless DC Motors. IV. Magnetic Field on Load. *IEEE Trans. Magn.* **1993**, *29*, 152–158. [CrossRef]
28. Ma, C.; Zuo, S. Black-Box Method of Identification and Diagnosis of Abnormal Noise Sources of Permanent Magnet Synchronous Machines for Electric Vehicles. *IEEE Trans. Ind. Electron.* **2014**, *61*, 5538–5549. [CrossRef]
29. Sahraoui, M.; Ghoggal, A.; Zouzou, S.E.; Benbouzid, M.E. Dynamic Eccentricity in Squirrel Cage Induction Motors-Simulation and Analytical Study of its Spectral Signatures on Stator Currents. *Simul. Model. Pract. Theory* **2008**, *16*, 1503–1513. [CrossRef]
30. Dorrell, D.G. Sources and Characteristics of Unbalanced Magnetic Pull in Three-Phase Cage Induction Motors with Axial-Varying Rotor Eccentricity. *IEEE Trans. Ind. Appl.* **2011**, *47*, 12–24. [CrossRef]
31. Hou, L.; Chen, Y.; Cao, Q.; Zhang, Z. Turning Maneuver Caused Response in an Aircraft Rotor-Ball Bearing System. *Nonlinear Dyn.* **2015**, *79*, 229–240. [CrossRef]
32. Genta, G. *Dynamics of Rotating Systems*; Springer: New York, NY, USA, 2005.
33. Zhang, Z.; Chen, Y.; Cao, Q. Bifurcations and Hysteresis of Varying Compliance Vibrations in the Primary Parametric Resonance for a Ball Bearing. *J. Sound Vib.* **2015**, *350*, 171–184. [CrossRef]
34. Tiwari, M.; Gupta, K.; Prakash, O. Effect of Radial Internal Clearance of a Ball, Bearing On the Dynamics of a Balanced Horizontal Rotor. *J. Sound Vib.* **2000**, *238*, 723–756. [CrossRef]



© 2018 by the authors. Licensee MDPI, Basel, Switzerland. This article is an open access article distributed under the terms and conditions of the Creative Commons Attribution (CC BY) license (http://creativecommons.org/licenses/by/4.0/).